scientific reports

OPEN

Low intensity UV driven dual functional Cu doped BiVO$_4$ for enhanced methylene blue degradation and *Staphylococcus aureus* inactivation

Thien Kuang Lih[1], Alvin Lim Teik Zheng[1,2✉], Hui Yan Tan[3], Shahrul Razid Sarbini[3], Kelly Wong Kai Seng[4], Eric Lim Teik Chung[5,6], Yoshito Andou[7,8] & Kar Ban Tan[9]

This study reported on a dual-functional Cu-doped BiVO$_4$ photocatalyst synthesized via the hydrothermal method. Optimized 1 wt% Cu doping narrowed the bandgap to 2.24 eV, enabling 85% methylene blue (MB) degradation under low-intensity UV (13 W) within 180 min; a 5.1-fold enhancement over bare BiVO$_4$. Radical trapping confirmed hydroxyl radicals ($\cdot$OH) and superoxide radicals ($\cdot$O$_2^-$) as the dominant reactive species. The catalyst retained > 92% efficiency over three cycles and exhibited moderate antibacterial activity against *Staphylococcus aureus* (12.6 ± 0.4 mm inhibition zone) in dark conditions, attributed to Cu^{2+} release. Cost analysis further revealed a competitive synthesis cost of approximately RM 7.57 per gram, supporting the economic viability for large-scale environmental remediation applications. The integration of dual photocatalytic and antibacterial functionalities, along with cost efficiency, reinforces the practical potential of Cu-doped BiVO$_4$ in wastewater treatment applications.

Keywords Bismuth vanadate, Copper doping, Hydrothermal, Photocatalysis, Antibacterial, Methylene blue

Dyes, used extensively in industries such as textiles, are not fully consumed during the dyeing process, leading to the discharge of toxic, carcinogenic, and mutagenic substances into water bodies. This pollution not only affects the quality of water but also disrupts aquatic life and increases the biological oxygen demand (BOD) and chemical oxygen demand (COD) of water bodies. The textile industry is the predominant contributor to dye effluent, accounting for approximately 54% of the total discharge[1,2]. Among the various dyes used, methylene blue (MB), a synthetic, heterocyclic aromatic compound (C$_{16}$H$_{18}$N$_3$SCl), is widely applied as a dye and colorant across multiple industrial sectors[2,3]. Photocatalysis has become a critical technology to address contemporary environmental challenges due to its potential to harness sunlight and convert it into usable energy forms, essential for pollution control via the generation of reactive oxygen species (ROS) that enable the oxidation or reduction of contaminants[4–8]. As a versatile and sustainable approach, photocatalysis can drive reactions that break down pollutants into harmless byproducts[7,9–11]. Despite considerable advancements, challenges persist in maximizing photocatalytic efficiency and scalability to enable broad application across different pollutants and environmental conditions. Many traditional metal oxide semiconductors such as TiO$_2$ and ZnO exhibit limitations when exposed to sunlight, primarily due to their wide band gaps that restrict visible light

[1]Department of Science and Technology, Faculty of Humanities, Management and Science, Universiti Putra Malaysia Sarawak, 97008 Bintulu, Sarawak, Malaysia. [2]Institute of Ecoscience Borneo, Universiti Putra Malaysia Sarawak, 97008 Bintulu, Sarawak, Malaysia. [3]Department of Crop Science, Faculty of Agricultural Science and Forestry, Universiti Putra Malaysia Sarawak, 97008 Bintulu, Sarawak, Malaysia. [4]Department of Agribusiness and Bioresource Economics, Faculty of Agriculture, Universiti Putra Malaysia, 43400 Serdang, Malaysia. [5]Department of Animal Science, Faculty of Agriculture, Universiti Putra Malaysia, 43400 Serdang, Malaysia. [6]Institute of Tropical Agriculture and Food Security, Universiti Putra Malaysia, 43400 Serdang, Malaysia. [7]Graduate School of Life Sciences and Systems Engineering, Kyushu Institute of Technology, Fukuoka 808-0196, Japan. [8]Collaborative Research Centre for Green Materials on Environmental Technology, Kyushu Institute of Technology, Fukuoka 808-0196, Japan. [9]Department of Chemistry, Faculty of Science, Universiti Putra Malaysia, 43400 Serdang, Selangor, Malaysia. ✉email: alvinltz@upm.edu.my

absorption[12,13]. This limitation has spurred a wave of interest in alternative semiconductors with narrower band gaps, which can absorb a broader range of the solar spectrum.

Bismuth vanadate (BiVO$_4$) is a promising semiconductor photocatalyst due to its ability to absorb visible light, chemical stability, and non-toxic nature[14–17]. Doping is a widely used strategy to enhance the photocatalytic performance of BiVO$_4$, a promising material for applications such as water splitting and pollutant degradation[18–20]. Previously, it was reported that doped BiVO$_4$ is effective in degrading various organic pollutants, including dyes, antibiotics and pesticides[21–23]. Various non-metal and metal elements have been explored for doping BiVO$_4$, each offering unique benefits in terms of charge separation, light absorption, and catalytic activity[9]. However, its photocatalytic efficiency is often limited by factors such as low charge separation efficiency and fast electron–hole recombination. Doping BiVO$_4$, by incorporating foreign atoms into its crystal lattice, strategically alters its electronic and structural properties, enhancing charge separation, extending light absorption, increasing surface area, and enabling defect engineering, thereby significantly improving its photocatalytic performance[24]. Among various potential dopants, copper (Cu) has attracted attention due to its compatibility with the BiVO$_4$ lattice and its ability to enhance charge transport properties. Incorporating Cu into BiVO$_4$ not only enables more effective light harvesting but also boosts the material's photocatalytic efficiency in pollutant degradation compared to other dopants. Previous studies have found that the doping with Cu ions at the Bi site of BiVO$_4$, due to their favourable electronic transition properties and energy levels, has been identified as an effective method for suppressing charge carrier recombination[25]. The introduction of Cu into BiVO$_4$ enhances its visible light absorption capabilities. This is attributed to the narrowing of the band gap, which allows for better utilization of the solar spectrum[26,27]. The degradation of pollutants by Cu-doped BiVO$_4$ involves the generation of ROS such as superoxide radicals ($\cdot O_2^-$) and hydroxyl radicals ($\cdot OH$). These species play a crucial role in breaking down organic contaminants[28].

Herein, Cu-doped BiVO$_4$ are developed via hydrothermal method, with an emphasis on exploring how varying concentrations of Cu influence the structural, morphological, and optical properties. By investigating these parameters, this study seeks to provide insights into optimizing photocatalytic efficiency for MB degradation under low power UV light, addressing key challenges in sustainable environmental applications.

Methodology
Materials
Analytical-grade chemicals were sourced for this study without further purification. The primary chemicals utilized for the synthesis included bismuth nitrate pentahydrate (Bi(NO$_3$)$_3$·5H$_2$O) and ammonium metavanadate (NH$_4$VO$_3$) obtained from Chemiz (M) Sdn. Bhd. Nitric acid (HNO$_3$), sodium hydroxide (NaOH), copper (II) sulfate pentahydrate (CuSO$_4$·5H$_2$O) and methylene blue (MB) were obtained from Bendosen Chemicals.

Preparation of BiVO$_4$ and Cu-doped BiVO$_4$
The hydrothermal synthesis approach was adopted to prepare both bare and Cu-doped BiVO$_4$ photocatalysts as shown in Fig. 1. To initiate the process, Bi(NO$_3$)$_3$·5H$_2$O was dissolved in a HNO$_3$ to form Solution A, while NH$_4$VO$_3$ was dissolved in NaOH to produce Solution B. Solution B was then slowly added to Solution A, leading to visible precipitation. The mixture, along with the precipitate, was transferred to a Teflon-lined autoclave, which was sealed and subjected to hydrothermal conditions at 180 °C for 15 h. Post-reaction, the precipitate was
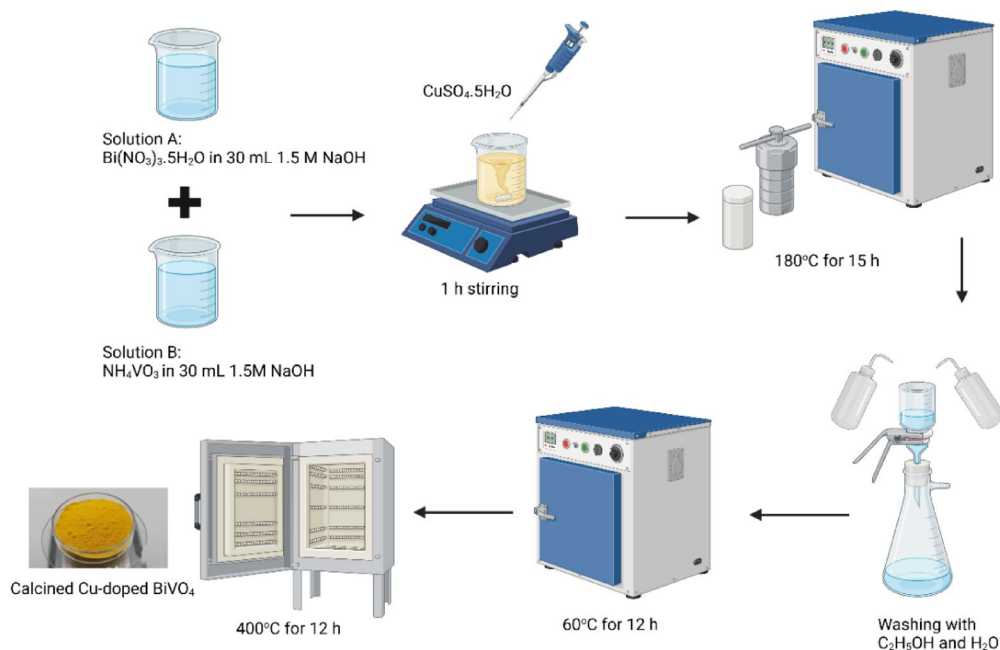

Fig. 1. The hydrothermal synthesis of Cu-doped BiVO$_4$. Drawn with BioRender.com.

washed with deionized water and ethanol, then dried at 60 °C for 12 h before being calcined at 400 °C to achieve phase purity. For Cu doping, varying concentrations of Cu precursor (1, 3, and 5 wt% relative to $BiVO_4$ mass) were introduced during the initial mixing stage.

Characterizations

The structural, chemical, morphological, and optical properties of the bare and Cu-doped $BiVO_4$ were comprehensively analyzed. X-ray diffraction (XRD) was employed to assess the crystallinity and phase structure with measurements conducted on a Shimadzu XRD6000 diffractometer with the measurement 2θ range of 10°–80° with a step size of 0.02° and a scanning speed of 1°/min. The morphology of the photocatalysts was accessed on a JCM-6000 Versatile Benchtop Scanning Electron Microscope, JEOL Ltd, Japan at 10 kV. FTIR was performed on an Agilent Cary 630 FTIR spectrometer with the KBr pellet method. Spectra were recorded over the 400–4000 cm^{-1} range with baseline and atmospheric corrections applied, identifying changes in functional groups due to Cu doping. The optical properties were accessed using UV–Visible spectroscopy and the optical band gap energies (E_g) were assessed using the Tauc plot.

Photocatalytic testing

The photocatalytic activity of the photocatalysts was evaluated using MB as the model pollutant. Briefly, suspension of photocatalyst is placed in MB solution and was stirred in the dark for 30 min to reach adsorption–desorption equilibrium before low intensity UV illumination. Aliquots were withdrawn every 20 min, centrifuged, and the residual MB concentration was measured using a UV–Vis spectrophotometer at 665 nm[29]. The calibration curve for MB is shown in Fig. S1. The photocatalytic degradation efficiency was calculated using the following equation:

$$\%Degradation = \frac{C_0 - C_t}{C_0} \times 100\%$$

where C_0 = initial concentration of MB; C_t = residual concentration of MB at 't' minute.

Anti-bacterial test

The synthesized 1% Cu-doped $BiVO_4$ was tested for their antibacterial activity using the disc diffusion method as previously reported[30,31]. The Gram-positive and Gram-negative bacteria that were employed were *Staphylococcus aureus* (*S. aureus*) and *Escherichia coli* (*E. coli*), respectively. Both gram-positive and gram-negative bacteria were cultured for a whole night at 37 °C in Lysogeny Broth (LB) medium. Mueller–Hinton agar plates were inoculated with bacterial suspensions at a density of 1.5×10^6 CFU/mL and turbidity of 0.5 McFarland standard. Ten sterile filter discs, each measuring 6 mm in diameter, were then impregnated with 1 mg/mL of 1% Cu-doped $BiVO_4$ suspension. Ethanol served as the negative control, and standard susceptibility discs containing chloramphenicol and streptomycin acted as the positive control. The inhibition zone (mm) of the 1% Cu-doped $BiVO_4$ was measured using a vernier calliper. The experimental results were expressed as mean ± standard deviation (SD) of five replicates.

Results and discussion

The crystalline structure and phase composition of the synthesized bare and Cu-doped $BiVO_4$ were analyzed using X-ray diffraction (XRD). As shown in Fig. 2a, all samples exhibited a monoclinic structure, with prominent peaks indexed to the (121) plane at a 2θ angle of approximately 28.9°, consistent with JCPDS no. 14-0688. The 1 wt% Cu-doped $BiVO_4$ showed a peak shift to higher 2θ angles, while higher Cu doping levels (3 wt% and 5 wt%) resulted in shifts to lower angles. These shifts are attributed to the substitution of Bi^{3+} ions (1.03 Å) with smaller Cu^{2+} ions (0.73 Å), causing lattice contraction. Conversely, the decrease in the diffraction angle at higher Cu doping levels may result from strain induced by the substitution of Cu^{2+} for V^{5+} ions, leading to localized lattice distortion and a slight expansion of the unit cell[32]. The disappearance of one of the low-angle peaks (< 20°) in Cu-doped samples compared to bare $BiVO_4$ can be attributed to lattice distortion and structural rearrangement caused by the substitution of Bi^{3+} with smaller Cu^{2+} ions, which suppresses or merges closely spaced crystal planes in this region[33]. Furthermore, the significant increase in peak intensity observed in the Cu-doped samples suggests improved crystallinity and possible preferential orientation induced by Cu incorporation during hydrothermal synthesis. The full-width at half-maximum (FWHM) values and corresponding crystallite sizes were calculated using the Scherrer equation (Table 1). The bare $BiVO_4$ exhibited the largest crystallite size (27.37 nm), while the 1 wt% Cu-doped $BiVO_4$ sample showed a reduced size (25.12 nm), indicating that Cu doping promotes defect formation and reduces particle aggregation. Crystallite size slightly increased at higher Cu doping levels (3 wt% and 5 wt%), likely due to the coalescence of smaller particles. The observed trends in peak shifts and crystallite size suggest a trade-off between lattice strain and defect generation with varying Cu doping concentrations.

The changes in lattice parameters confirm the effective incorporation of Cu ions into the $BiVO_4$ lattice, thereby modifying its electronic and structural properties, which are crucial for optimizing photocatalytic performance.

The functional groups and lattice vibrations of the synthesized bare and Cu-doped $BiVO_4$ samples were analyzed using Fourier transform infrared (FTIR) spectroscopy, as shown in Fig. 3.

The FTIR spectra revealed characteristic vibrational bands corresponding to $BiVO_4$ with specific attention to the V–O bond vibrations within the VO_4 tetrahedral structure. Peaks were observed in the range of 750–900 cm^{-1}, consistent with the stretching modes of V–O bonds[34]. The wavenumber shifts in this region were notable as shown in the inset of Fig. 3, with bare $BiVO_4$ showing a peak at 728.69 cm^{-1}, while Cu-doped $BiVO_4$ samples exhibited peaks at 730.56 cm^{-1} (1 wt% and 3 wt%) and 724.97 cm^{-1} (5 wt%). These shifts are attributed
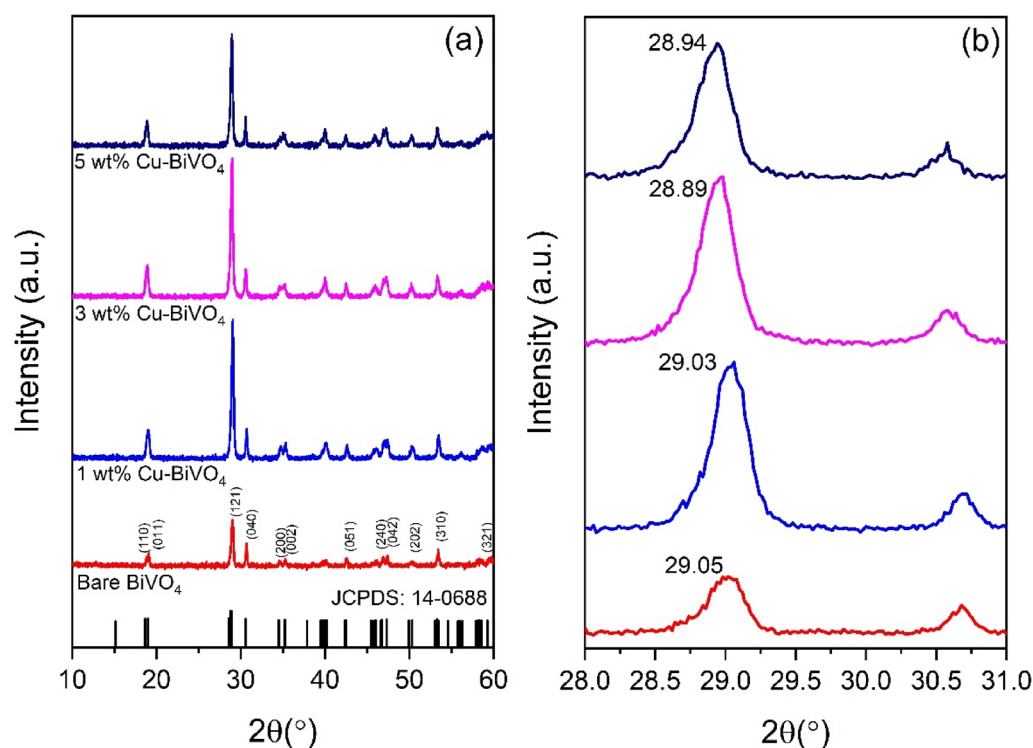
Fig. 2. (**a**) XRD analysis of bare and Cu-doped $BiVO_4$. (**b**) Magnified view of the (121) diffraction peak showing shifts with Cu doping.

Sample	FWHM	Crystalline size (nm)	Lattice strain
Bare $BiVO_4$	0.3045	27.37	0.0259
1 wt% Cu- $BiVO_4$	0.3881	25.12	0.0352
3 wt% Cu- $BiVO_4$	0.3586	29.10	0.0332
5 wt% Cu- $BiVO_4$	0.3551	28.88	0.0334

Table 1. FWHM value and crystalline size for bare and Cu-doped $BiVO_4$.

to distortions in the $BiVO_4$ lattice caused by the substitution of Cu^{2+} ions for Bi^{3+} or V^{5+} ions. The ionic radius mismatch between Cu^{2+} (0.73 Å) and Bi^{3+} (1.03 Å) induces lattice strain and creates oxygen vacancies, altering the vibrational environment and leading to the observed peak shifts. Additionally, broader and more intense peaks in the Cu-doped samples suggest the formation of oxygen vacancies and changes in bond strength due to the doping process. The presence of oxygen vacancies enhances the local electronic environment, potentially improving charge separation and photocatalytic activity.

The morphology and surface characteristics of the synthesized bare and Cu-doped $BiVO_4$ were examined using scanning electron microscopy (SEM). As depicted in Fig. 4a, bare $BiVO_4$ displayed irregularly shaped particles with relatively large sizes and a rough surface morphology, ranging from near-spherical to polyhedral structures. The particles exhibited a loosely packed arrangement with limited porosity. In comparison, the Cu-doped $BiVO_4$ as shown in Fig. 4b–d showed significant changes in morphology. The particle size decreased progressively with Cu doping, particularly in the 1 wt% Cu-doped $BiVO_4$, which exhibited the smallest and most uniformly distributed particles. This reduction in size is attributed to Cu-induced lattice distortion, which inhibits particle aggregation during synthesis. Although BET and BJH pore size distribution analyses are absent in this study, analogous hydrothermally synthesized Cu-doped $BiVO_4$ systems have been reported to demonstrate increased mesoporosity and surface roughness, attributable to lattice distortion and reduced particle aggregation[27]. These morphological alterations are claimed to enhance the accessibility of reactive sites, thereby correlating with the improved photocatalytic performance observed in this study.

Enhanced porosity likely increases the surface area, which is advantageous for catalytic applications requiring efficient interfacial interactions.

The incorporation of Cu atoms within the $BiVO_4$ lattice was visually evident, particularly in the 1 wt% Cu-doped sample (Fig. 4b), where the Cu distribution appeared homogeneous across the catalyst surface. Higher Cu doping levels (3 wt% and 5 wt%) resulted in observable clustering, which could be attributed to excess
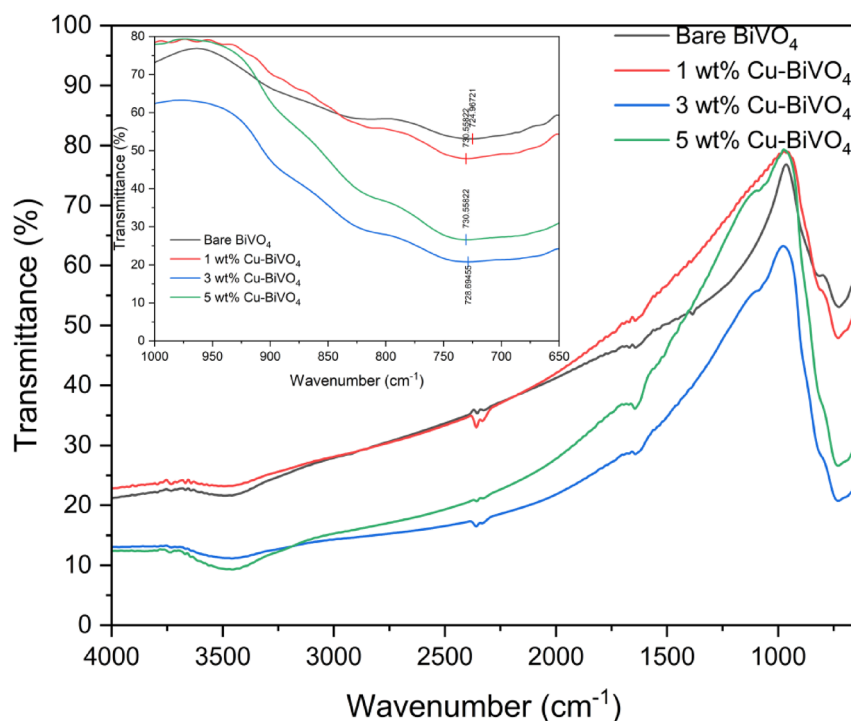
Fig. 3. FTIR spectra of bare and Cu-doped $BiVO_4$ with varying Cu contents (1 wt%, 3 wt%, and 5 wt%). *Inset:* Enlarged view of the 650–1000 cm^{-1} region.

Cu species forming separate phases or aggregates, potentially reducing photocatalytic efficiency as shown in Fig. 4c and d, respectively. Overall, the SEM analysis highlights that Cu doping significantly impacts particle size, morphology, and surface structure. These morphological changes contribute to an increased active surface area and improved photocatalytic performance, particularly for the 1 wt% Cu-doped $BiVO_4$, which demonstrates an optimal balance between porosity, particle size, and structural integrity. The incorporation of Cu into the $BiVO_4$ lattice is supported by XRD peak shifts (Fig. 2) and FTIR band changes (Fig. 3), indicating lattice contraction and modifications in the local bonding environment. The SEM images reflect morphological changes associated with Cu doping but do not provide direct evidence of atomic-level incorporation. The observed highly porous surface morphology in the prepared samples aligns with crystallite size calculations derived from XRD analysis and previous studies on Cu-doped $BiVO_4$, which reported suppressed particle growth and enhanced size uniformity. These findings are consistent with prior high-resolution transmission electron microscopy (HRTEM) investigations of Cu-doped $BiVO_4$, which confirmed dopant-induced structural modifications[35].

The band gap energies (E_g) were estimated via Tauc plots, as shown in Fig. 5. The E_g for bare $BiVO_4$ was calculated to be 2.88 eV, consistent with its known optical characteristics. Cu doping significantly influenced the band gap energies. The 1 wt% Cu-doped $BiVO_4$ showed the lowest band gap of 2.24 eV, representing a substantial narrowing compared to the bare sample. This reduction enhances visible light absorption, facilitating more effective electron excitation and increasing the generation of electron–hole pairs, which are critical for photocatalytic activity. The observed narrowing of the band gap is attributed to the introduction of intermediate energy levels by Cu ions, which modify the electronic structure of $BiVO_4$. The smaller band gap facilitates electron excitation, leading to more effective generation of electron–hole pairs for photocatalysis as the ability to absorb light is enhanced due to the broaden region of electromagnetic wave that could excite the electron[36]. Interestingly, as the Cu doping concentration increased to 3 wt% and 5 wt%, the band gap energy increased slightly to 2.55 eV and 2.44 eV, respectively. This trend suggests that excessive doping introduces structural distortions and defect states, which may partially hinder light absorption. Similar trends have been observed in other studies where excessive dopant concentrations lead to the aggregation of dopant species, altering the electronic band structure and reducing photocatalytic performance[37,38]. The band gap narrowing observed at optimal doping levels (1 wt%) enhances light utilization across a broader spectrum, making the material more efficient under low-intensity UV light.

This anomaly can be explained by the interplay between defect-related and structural effects. At lower Cu concentrations, substitutional Cu^{2+} ions introduce shallow defect states and oxygen vacancies, which effectively narrow the band gap and improve visible light absorption. However, at higher Cu loadings, excessive doping may lead to local lattice distortions or dopant clustering, creating deep-level defect states that trap carriers without contributing to photocatalytically active transitions[39]. These competing effects result in a non-monotonic variation in band gap with increasing Cu content.

While a more comprehensive evaluation of band gap energies via diffuse reflectance spectroscopy (DRS) utilizing the Kubelka–Munk function was precluded by instrumental constraints, the observed band gap
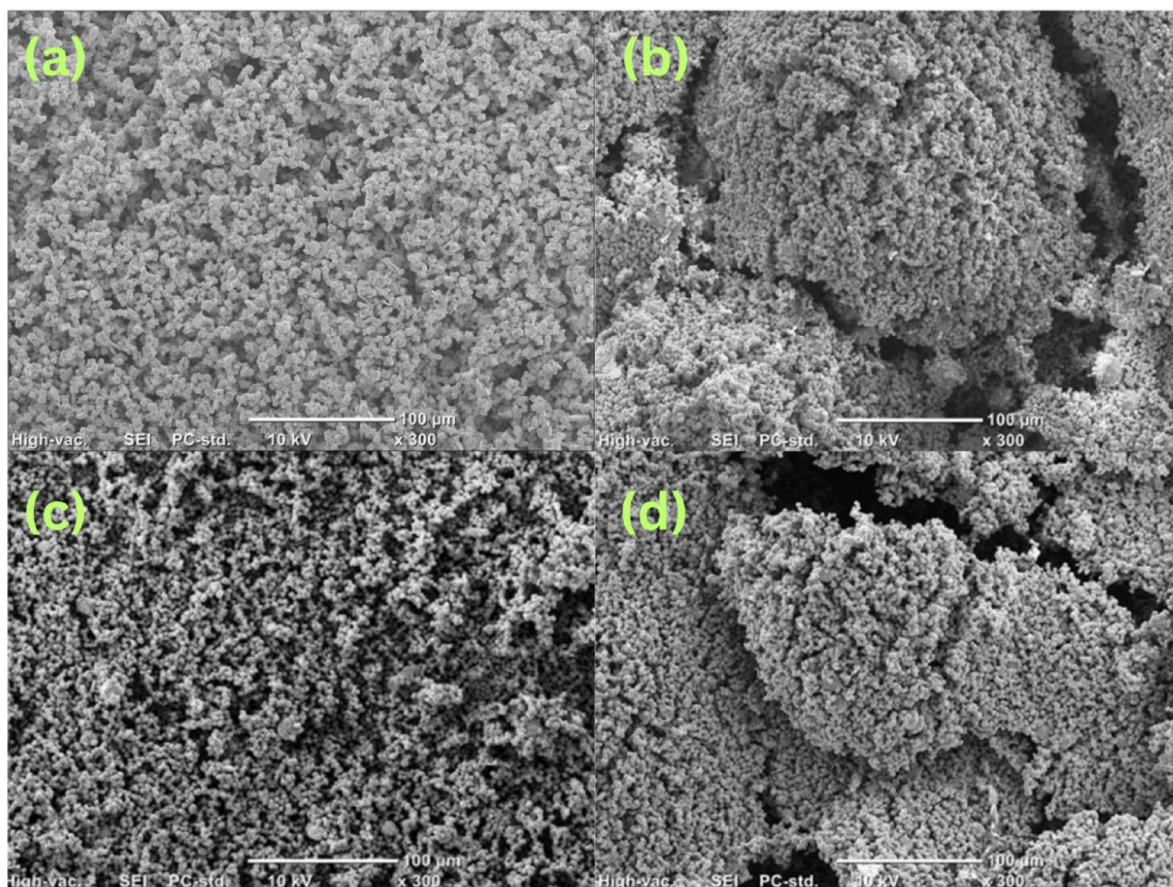
Fig. 4. SEM images of (**a**) bare BiVO$_4$, (**b**) 1 wt% Cu–BiVO$_4$, (**c**) 3 wt% Cu–BiVO$_4$, and (**d**) 5 wt% Cu–BiVO$_4$ at 300× magnification.
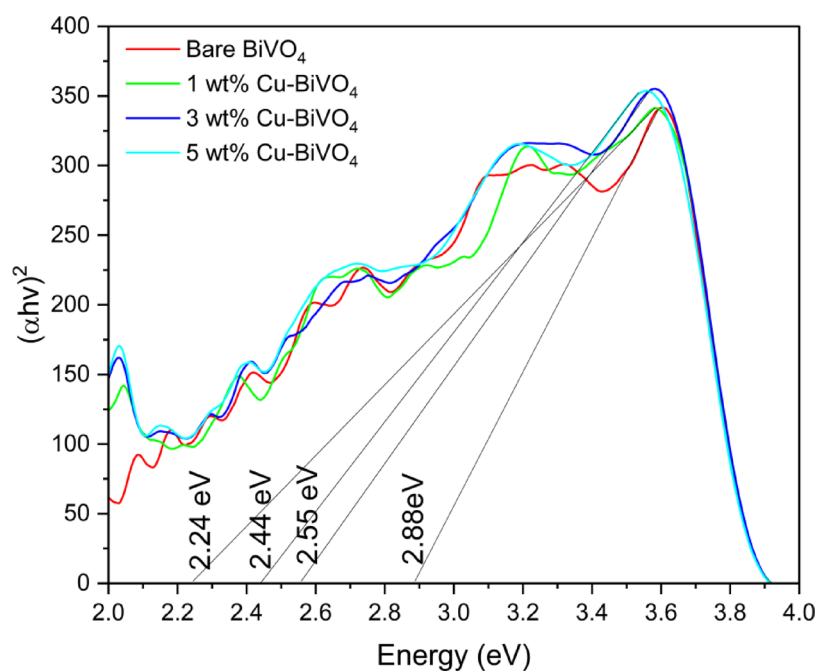

Fig. 5. Band gap energy estimation using Tauc plot.

narrowing in our current study demonstrates consistency with prior DRS-based investigations of Cu-doped $BiVO_4$, which reported reductions to 2.2–2.4 eV dependent on Cu concentration[40,41]. Furthermore, despite the absence of direct evidence from photoluminescence (PL), photocurrent response, or electrochemical impedance spectroscopy (EIS) within this study, the observed band gap narrowing, crystallite size reduction, and enhanced photocatalytic activity are consistent with prior reports indicating that Cu doping in $BiVO_4$ significantly enhances charge separation and transfer characteristics[41]. These correlations suggest that Cu incorporation enhances both the electronic and surface properties of $BiVO_4$, thereby contributing to the improved photocatalytic performance observed in this investigation.

The photocatalytic activity of bare and Cu-doped $BiVO_4$ samples was evaluated using MB degradation, as shown in Fig. 6a. A preliminary adsorption test was conducted by stirring the catalyst-MB solution in the dark for 30 min to achieve adsorption–desorption equilibrium. The results indicate that adsorption performance was relatively low for all samples, with the highest adsorption observed for the 3 wt% Cu-doped $BiVO_4$ at approximately 8%. This suggests that the degradation efficiency of the catalyst under UV light is primarily due to photocatalytic activity rather than physical adsorption of MB. Control experiments revealed that MB photolysis in the absence of a catalyst was negligible, with no significant degradation observed under UV light over 180 min. This confirms the essential role of the catalyst in facilitating the photodegradation of MB. Among the samples, the 1 wt% Cu-doped $BiVO_4$ achieved the highest MB degradation efficiency, exceeding 85% after 180 min. The bare $BiVO_4$, by comparison, degraded only 8% of MB under identical conditions. The enhanced performance of the 1 wt% Cu-doped $BiVO_4$ is attributed to its optimized band gap energy (2.24 eV), improved light absorption, and effective charge separation, which facilitate the generation of ROS. As the Cu doping concentration increased to 3 wt% and 5 wt%, the degradation efficiency declined, likely due to excessive dopant-induced defects and clustering, which hinder light absorption and electron–hole pair separation. The degradation kinetics were analyzed using the pseudo-first-order (PFO) model, as shown in Fig. 6b. The calculated rate constant (k) for the 1 wt% Cu-doped $BiVO_4$ was 0.00306 min^{-1}, representing a 8.8-fold increase compared to the bare $BiVO_4$, which had a rate constant of 0.000346 min^{-1}. This dramatic improvement highlights the critical role of Cu doping in enhancing photocatalytic performance by improving charge carrier dynamics and promoting the generation of ROS. For higher Cu doping concentrations, the rate constants were 0.000734 min^{-1} (3 wt%) and 0.00119 min^{-1} (5 wt%), corresponding to 2.1-fold and 3.44-fold increases, respectively, relative to the bare $BiVO_4$. These findings emphasize that while Cu doping is essential for enhancing photocatalytic activity, excessive doping can introduce detrimental effects, such as defect-induced recombination and reduced light absorption. Similar pattern was observed in which the rate constant initially increased and subsequently decreased for the degradation of Rhodamine B using Cu-doped $BiVO_4$[35].

The initial pH of the solution plays a key role in photocatalytic processes, as it influences the degradation of dye molecules by affecting the surface electrical charge properties of the catalyst[42]. The pH value also affects the dissociation ability of compounds, the charge distribution on the catalyst surface, and the oxidation potential of the catalyst's VB[43]. The influence of pH on the photocatalytic degradation of MB using 1 wt% Cu-doped
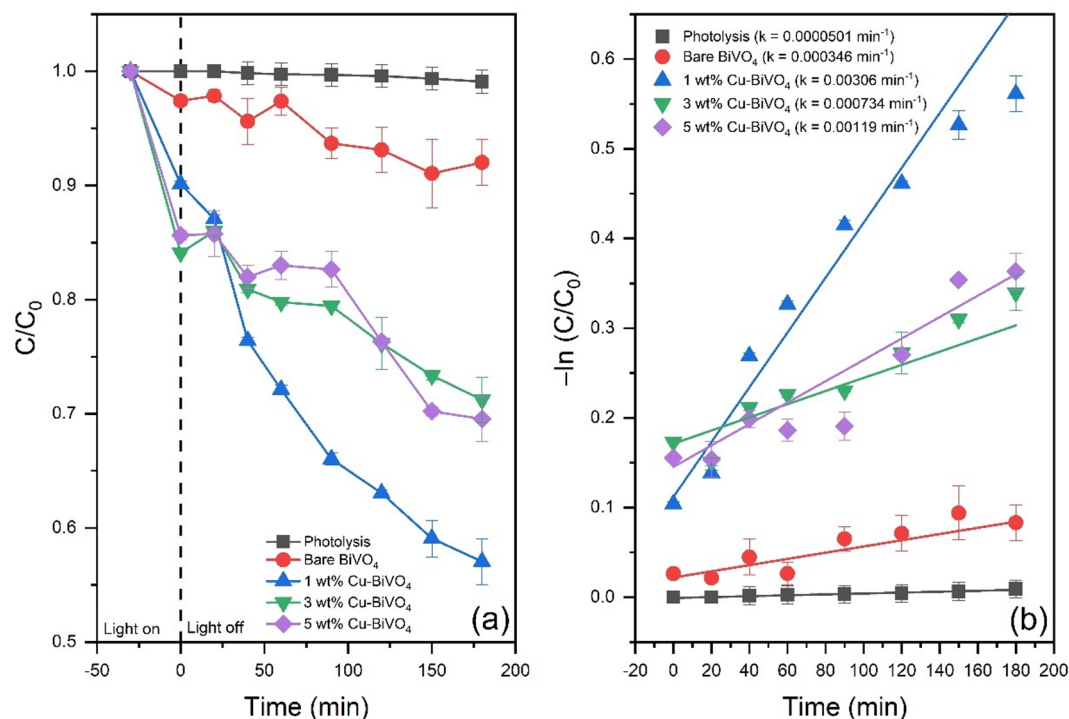

Fig. 6. (**a**) Photocatalytic degradation of MB using bare and Cu-doped $BiVO_4$. (**b**) pseudo-first-order kinetic plots ($-\ln(C/C_0)$ versus time). Error bars represent the standard deviation (SD) from triplicate measurements.

BiVO$_4$ was investigated. . Fig. 7a shows the degradation efficiencies at three distinct pH levels: acidic (pH 4.7), near-neutral (pH 6.25), and basic (pH 9.7). The results reveal that basic conditions (pH 9.7) yielded the highest degradation efficiency, achieving 62% MB degradation within 180 min. In comparison, the near-neutral condition (pH 6.25) and acidic condition (pH 4.7) resulted in efficiencies of 43% and 13%, respectively. The superior performance under basic conditions is attributed to the favorable surface charge properties of the catalyst and the enhanced generation of ·OH. At pH values above the isoelectric point of BiVO$_4$ (approximately pH 3.4), the catalyst surface becomes negatively charged, facilitating the adsorption of positively charged MB molecules and promoting ROS generation. The presence of these radicals is enhanced in alkaline environments, leading to more effective breakdown of MB molecules[44]. Conversely, under acidic conditions, the catalyst surface is predominantly positively charged, leading to electrostatic repulsion between the catalyst and MB molecules. Additionally, the excess protons (H$^+$) in acidic media can scavenge ·OH, reducing their availability for MB degradation. The degradation kinetics at different pH levels were analyzed using the PFO model, as shown in Fig. 7b. The calculated rate constant (k) was highest under basic conditions (k = 0.00764 min^{-1}), followed by near-neutral (k = 0.00264 min^{-1}) and acidic conditions (k = 0.000613 min^{-1}). The rate constant under basic conditions exhibited a 12.5-fold increase compared to acidic conditions, demonstrating the significant impact of pH on photocatalytic performance.

In this study, three different catalyst loadings of 1 wt% Cu-doped BiVO$_4$ were investigated: 50 mg, 100 mg, and 200 mg in 100 mL of MB solution. The results presented in Fig. 8a indicate a direct correlation between the amount of catalyst used and the efficiency of the photocatalytic degradation process. Increasing the catalyst loading from 50 to 200 mg led to a significant improvement in degradation efficiency. At 50 mg, MB degradation efficiency was approximately 38%, which increased to 62% and 85% for 100 mg and 200 mg, respectively, after 180 min. The enhanced performance with higher catalyst loading is attributed to the increased availability of active sites, which facilitates greater generation of ROS and accelerates the photocatalytic degradation process. However, further increases in catalyst loading beyond 200 mg may lead to diminishing returns due to excessive turbidity in the reaction mixture. However, beyond a certain threshold, further increases can reduce efficiency due to increased turbidity, which scatters light and diminishes its effectiveness[45]. Although further increases in catalyst loading beyond 200 mg were not tested in this study, previous reports indicate that excessive catalyst concentrations can lead to increased turbidity and particle agglomeration, which scatter light and reduce effective photon penetration, ultimately diminishing photocatalytic efficiency[46]. The degradation kinetics were analyzed using the PFO model, as shown in Fig. 8b. The rate constant (k) increased with catalyst loading, with values of 0.00524 min^{-1} for 50 mg, 0.00757 min^{-1} for 100 mg, and 0.00741 min^{-1} for 200 mg. The results indicate that increasing the catalyst loading from 50 to 200 mg resulted in a 1.4-fold increase in the rate constant. This trend highlights the direct relationship between catalyst loading and the rate of photocatalytic reactions.

The impact of initial MB concentration on photocatalytic degradation efficiency was evaluated using 1 wt% Cu-doped BiVO$_4$ under low-intensity UV light (13 W). Initial MB concentrations of 5 mg/L, 10 mg/L, and 20 mg/L were tested, with the results presented in Fig. 9a. The degradation efficiency decreased as the initial MB concentration increased, highlighting the inverse relationship between MB concentration and photocatalytic
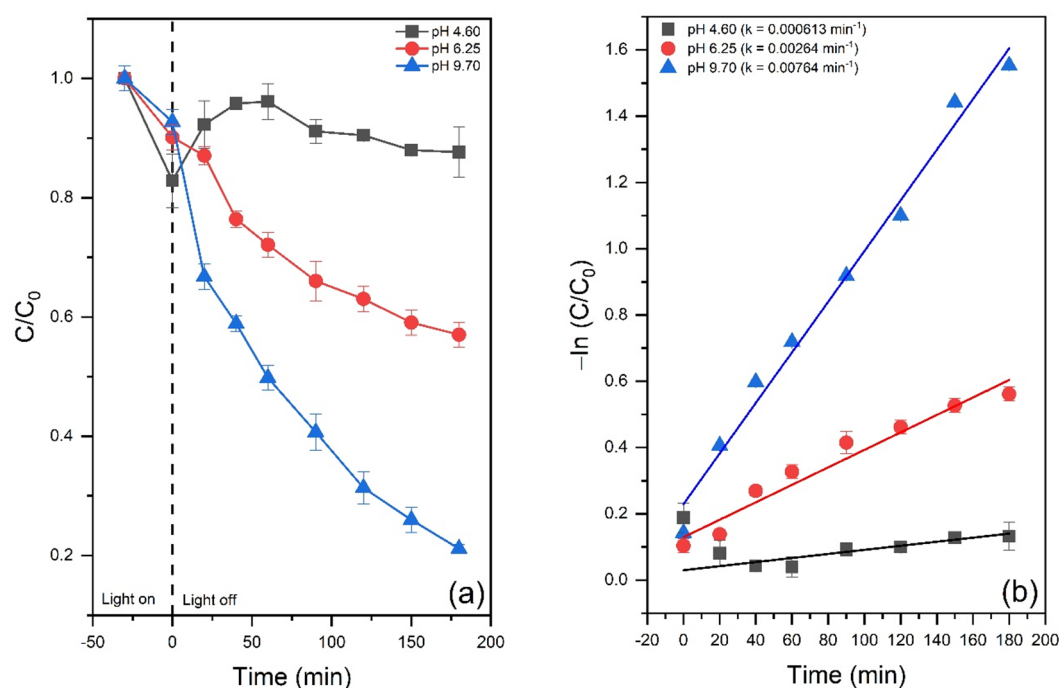

Fig. 7. (**a**) Effect of solution pH on MB degradation. (**b**) pseudo-first-order kinetic plots ($-\ln(C/C_0)$ versus time). Error bars represent the standard deviation (SD) from triplicate measurements.
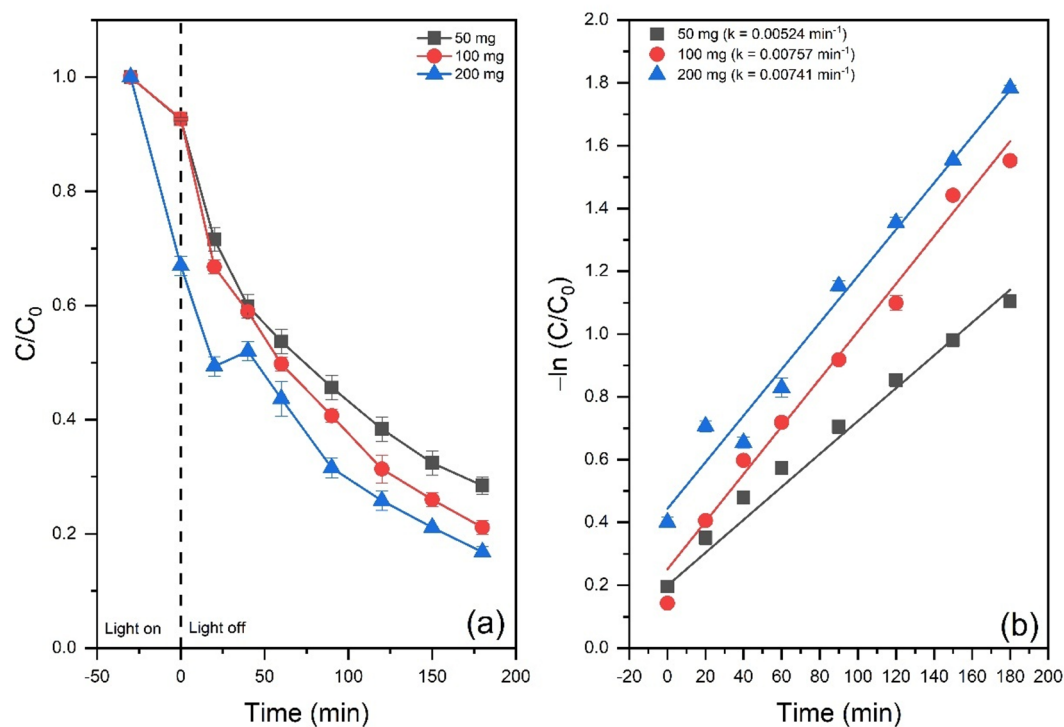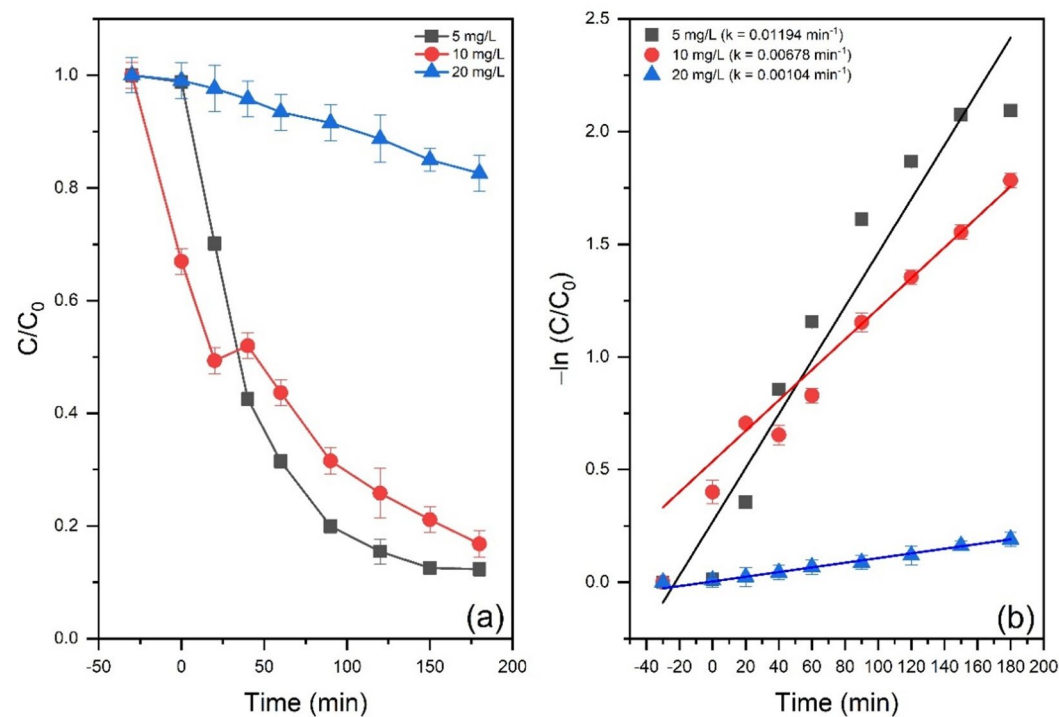
Fig. 8. (**a**) Effect of catalyst loading on MB degradation. (**b**) pseudo-first-order kinetic plots ($-\ln(C/C_0)$ versus time). Error bars represent the standard deviation (SD) from triplicate measurements.

Fig. 9. (**a**) Effect of initial MB concentration on MB degradation. (**b**) pseudo-first-order kinetic plots ($-\ln(C/C_0)$ versus time). Error bars represent the standard deviation (SD) from triplicate measurements.

performance. At 5 mg/L, the photocatalytic efficiency reached approximately 85% within 180 min. However, at 10 mg/L and 20 mg/L, the efficiencies dropped to 79% and 17%, respectively. The reduced performance at higher concentration (20 mg/L) is attributed to the increased number of MB molecules competing for the available ROS and active sites on the catalyst surface. Additionally, higher concentrations result in greater light absorption by the MB itself, limiting the photons available to excite the catalyst and reducing the generation of electron–hole pairs[47]. It is noted that the apparent adsorption of MB in the dark for the 10 mg/L solution was slightly higher than the other concentrations, which may reflect minor experimental variability in catalyst dispersion or adsorption kinetics during the equilibrium stage. This does not significantly impact the overall trend, as photocatalytic degradation under UV irradiation remains the dominant mechanism for MB removal across all concentrations tested.

The degradation kinetics for varying initial MB concentrations were analyzed using the PFO model, as shown in Fig. 9b. The calculated rate constants (k) were 0.01194 min^{-1} for 5 mg/L, 0.00684 min^{-1} for 10 mg/L, and 0.00104 min^{-1} for 20 mg/L. These results indicate a 2.7-fold decrease in the rate constant when the MB concentration increased from 5 to 20 mg/L. This trend confirms that higher MB concentrations impede the photocatalytic process by limiting the availability of active sites and reducing the penetration of light into the solution. The observed decline in photocatalytic efficiency and reaction rates with increasing MB concentration is consistent with previous studies[48,49].

Radical trapping experiments were conducted to identify the primary ROS responsible for the photocatalytic degradation of MB. Methanol, ascorbic acid (AA), ethylenediaminetetraacetic acid (EDTA), and tert-butanol (Tert-OH) were employed as scavengers for $\cdot OH$, $\cdot O_2^-$, and h^+, respectively[50]. The results are summarized in Fig. 10. The addition of methanol significantly suppressed MB degradation, confirming that $\cdot OH$ play a crucial role in the photocatalytic process. Similarly, AA, a scavenger for $\cdot O_2^-$, caused a substantial reduction in photocatalytic activity, indicating that $\cdot O_2^-$ is also a key reactive species. The introduction of EDTA, which acts as an h^+ scavenger, moderately inhibited the degradation efficiency, suggesting that h^+ contribute to the reaction but are less significant than $\cdot OH$ and $\cdot O_2^-$. The moderate suppression observed with Tert-OH further highlights the importance of $\cdot OH$ in the degradation process. Interestingly, methanol showed stronger inhibition compared to Tert-OH, which can be attributed to its dual role as both a $\cdot OH$ scavenger and a h^+ scavenger, making it more effective in quenching the reactive species involved in the photocatalytic mechanism[51]. The results of the trapping experiments confirm that $\cdot OH$ and $\cdot O_2^-$ are the primary ROS responsible for MB degradation, with $\cdot OH$ being slightly more dominant.

The stability and reusability of the 1 wt% Cu-doped $BiVO_4$ catalyst were assessed through three consecutive photocatalytic degradation cycles as shown in Fig. 11. Following each cycle, the photocatalysts underwent a washing process with deionized water and ethanol, subsequently being dried at 80 °C prior to subsequent usage. In the first cycle, the MB degradation efficiency reached 85.6%. However, a slight decline was observed in subsequent cycles, with efficiencies of 81.8% and 78.9% recorded for the second and third cycles, respectively.
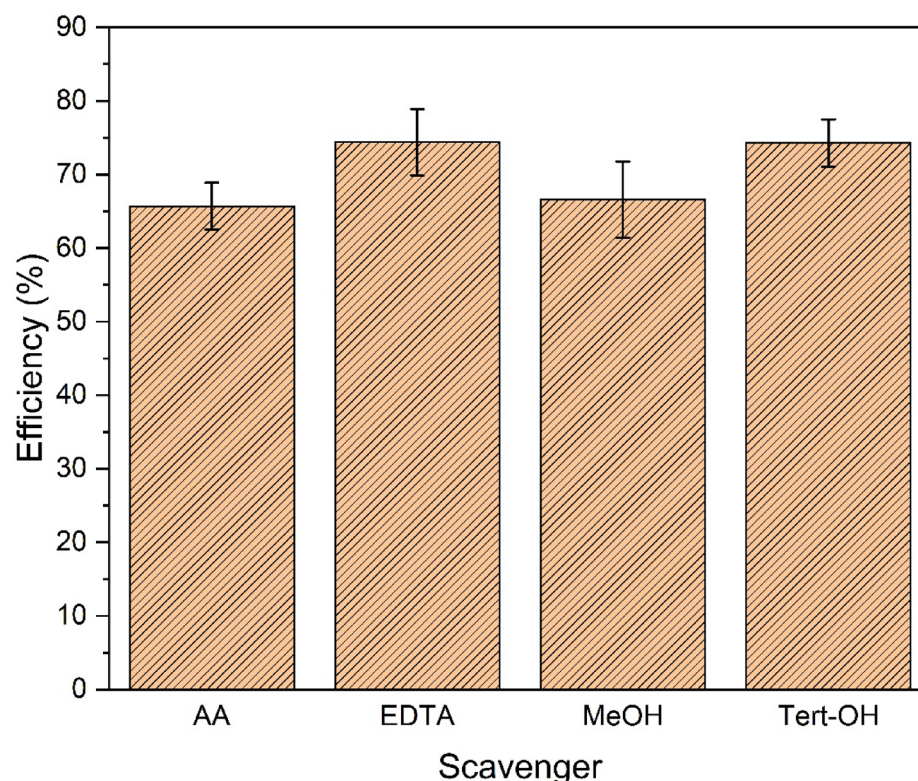

Fig. 10. Radical trapping test. Error bars represent the standard deviation (SD) from triplicate measurements.
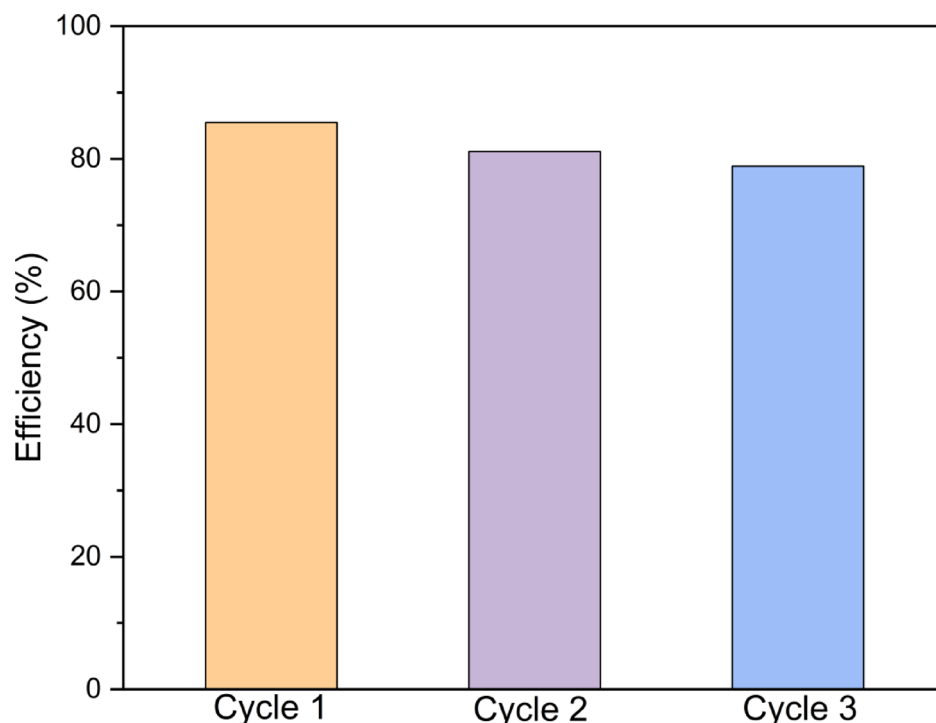
Fig. 11. Recycling tests of 1 wt% Cu-doped $BiVO_4$ for MB degradation.

This corresponds to a total reduction of 6.7% in photocatalytic performance over three cycles, indicating excellent stability and reusability of the catalyst. The gradual decline in efficiency can be attributed to the adsorption of degradation byproducts on the catalyst's active sites, a phenomenon known as catalytic poisoning[52]. These byproducts may block the active sites and hinder the catalyst's ability to facilitate photocatalytic reactions. Chemical characterization of the recycled catalyst, as shown in Fig. S2, revealed minor changes in the FTIR spectra, including a slight shift in the V–O vibrational peak from 730.56 cm to 728.69 cm^{-1}, which can be attributed to the adsorption of organic residues. While XPS analysis before and after photocatalytic use could not be performed in this study due to instrumentation constraints, the excellent reusability performance (> 92% retained activity over three cycles) suggests structural and chemical stability of the catalyst.

Possible photodegradation mechanism of MB

A possible photocatalytic degradation mechanism for MB using 1 wt% Cu-doped $BiVO_4$ under low-intensity UV light irradiation can be proposed, $_4$ as shown in Fig. 12.

The proposed photocatalytic mechanism involves several interconnected steps: (1) Cu doping reduces the $BiVO_4$ band gap from 2.88 to 2.24 eV, enhancing light absorption and promoting electron excitation from the VB to the CB; (2) Cu ions act as electron traps, facilitating charge separation and suppressing recombination; (3) photogenerated electrons react with dissolved O_2 to produce $\cdot O_2^-$ radicals, while holes oxidize water or OH^- to form $\cdot OH$ radicals; (4) these ROS attack MB molecules, leading to stepwise demethylation, aromatic ring cleavage, and mineralization. The dominance of $\cdot OH$ and $\cdot O_2^-$ species is corroborated by radical scavenging experiments (Fig. 10), which showed substantial suppression of MB degradation upon the addition of methanol and ascorbic acid.

Similar findings have been reported in other doped ternary oxide systems. For instance, Mg-doped Zn_2SnO_4 exhibited a substantial band gap reduction (3.82–3.74 eV) and a significant increase in surface area, with oxygen vacancies playing a critical role in enhancing ROS generation and pollutant degradation efficiency[53]. Likewise, Ba-alloyed Zn_2SnO_4 demonstrated that dopant incorporation induces compressive strain and creates additional defect states, leading to improved charge transfer and higher $\cdot OH$ radical production[54]. These observations align with our radical scavenger results (Fig. 10), confirming that $\cdot OH$ radicals are the dominant reactive species in Cu-doped $BiVO_4$ photocatalysis and highlighting the crucial role of defect engineering in boosting photocatalytic efficiency.

1. *Photoexcitation*:

$$Cu\text{-}BiVO_4 + h\nu \,(UV \text{ light}) \,\rightarrow\, Cu\text{-}BiVO_4 \left(e^- + h^+\right)$$
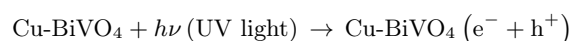
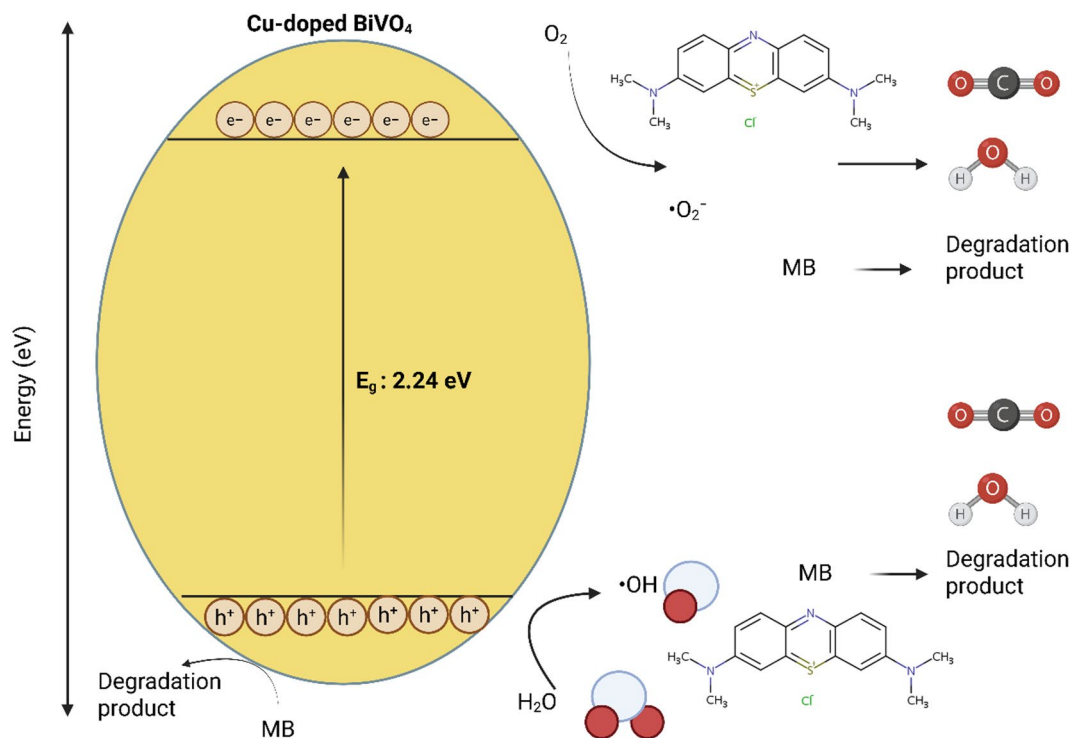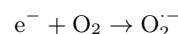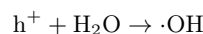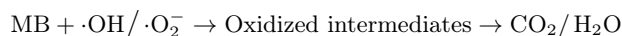2. *Charge separation enhancement by Cu doping*:

Fig. 12. Proposed MB degradation mechanism on 1 wt% Cu-doped $BiVO_4$. Drawn with BioRender.com.

Cu doping reduces electron-hole recombination, improving the efficiency of charge carriers.

3. *Reactive species formation*:

$$h^+ + H_2O \rightarrow \cdot OH$$

$$e^- + O_2 \rightarrow O_2^{\cdot-}$$

4. *Degradation of MB*:

$$MB + \cdot OH / \cdot O_2^- \rightarrow \text{Oxidized intermediates} \rightarrow CO_2/H_2O$$

Although LC–MS or HPLC analysis could not be conducted in this study to experimentally confirm intermediates, the proposed pathway aligns with findings from previous photocatalytic studies where MB degradation intermediates, such as azure A/B/C, thionine, and demethylated aromatic fragments, were identified using LC–MS and HPLC analyses[55,56]. Herein, the proposed degradation pathway of MB likely involves multiple oxidative and reductive processes mediated by ROS such as $\cdot OH$ and $\cdot O_2^-$ as previously reported[57,58]. These processes initiate bond cleavage in the MB molecule, leading to the formation of intermediate organic compounds, which subsequently degrade into inorganic end-products such as CO_2, H_2O, Cl^-, SO_4^{2-}, and NO_3^-. The degradation process begins with the cleavage of the N–CH_3 bond, as it has one of the lowest bond dissociation energies. The methyl groups (–CH_3) are oxidized to formaldehyde (HCHO) or formic acid (HCOOH). Concurrently, oxidation reactions lead to the conversion of sulfur-containing groups in MB, such as Cl–S groups, into sulfoxide (S=O) and sulfone species, destabilizing the central aromatic structure of the dye molecule. For example, $\cdot OH$ radicals attack the heteroaromatic ring and sulfur groups, resulting in the opening of the central aromatic structure and the formation of smaller organic compounds. Similar studies have identified key intermediates such as azure A, azure B, azure C, and thionine during MB degradation[59]. These intermediates confirm the stepwise cleavage of bonds in the MB molecule, leading to simpler fragments. The heteroaromatic rings undergo successive oxidations and bond cleavages. The C–S bonds and remaining C–N bonds are progressively broken, resulting in the dissociation of the aromatic rings into simpler structures. Sulfur-containing intermediates are further oxidized to sulfate ions (SO_4^{2-}), while nitrogen-containing intermediates oxidize to nitrate ions (NO_3^-) and ammonium (NH_4^+). As the degradation progresses, the remaining organic intermediates are oxidized into smaller volatile molecules, including CO_2 and H_2O. Simultaneously, mineral ions such as Cl^-, SO_4^{2-}, and NO_3^- are released into the solution. Although no specific experiments were conducted in this study to confirm these intermediates, the proposed pathway aligns with findings from similar photocatalytic studies.

Comparison with previous study

Previous literature on $BiVO_4$-based photocatalysts has demonstrated significant advancements in dye degradation under various conditions as shown in Table 2. For example, Fe-loaded $BiVO_4$ achieved an impressive 81% degradation of MB within 30 min under visible light[60], while rGO/$BiVO_4$ BiPO exhibited 94.4% degradation efficiency at pH 9 under similar light conditions[61]. Other studies reported modifications such as Mo-doping, which enabled 88.57% degradation of MB within 120 min under visible light. These findings highlight the effectiveness of doping strategies and structural modifications in enhancing the photocatalytic performance of $BiVO_4$. In comparison, the current study achieved 85% MB degradation within 180 min using 1 wt% Cu-doped $BiVO_4$ under a low-intensity UV lamp (13 W). This result is particularly notable as it was accomplished with significantly lower energy requirements compared to studies utilizing high-energy light sources. Additionally, the hydrothermal synthesis method employed here is both simple and cost-effective, offering scalability without sacrificing performance. The reduced band gap energy (2.24 eV) and improved charge separation achieved through Cu doping further highlight the advancements in photocatalytic efficiency introduced by this study. Beyond photocatalytic performance, this work distinguishes itself by demonstrating the dual functionality of Cu-doped $BiVO_4$. While most prior studies focus solely on pollutant degradation, the antibacterial activity of Cu-doped $BiVO_4$ against *S. aureus* in dark conditions provides an added advantage. This dual functionality addresses both organic pollutant degradation and microbial contamination, making it a versatile material for environmental remediation. In summary, the findings of this study not only surpass the degradation efficiency of many previously reported $BiVO_4$-based photocatalysts under low-energy conditions but also introduce novel functionalities and operational efficiencies. The dual-purpose capability and scalable synthesis approach position Cu-doped $BiVO_4$ as a promising candidate for practical applications in wastewater treatment and environmental remediation.

Cost analysis

The economic viability of synthesizing Cu-doped $BiVO_4$ photocatalysts for practical applications was evaluated by analyzing the costs associated with raw materials, synthesis methods, and potential scalability. The synthesis of 1 wt% Cu-doped $BiVO_4$ was evaluated for cost efficiency, yielding approximately 3.5 g of the catalyst at a total production cost of RM 26.48, which corresponds to RM 7.57 per gram. The primary chemicals used in synthesizing Cu-doped $BiVO_4$, including $Bi(NO_3)_3 \cdot H_2O$, NH_4VO_3, and $CuSO_4 \cdot 5H_2O$, are relatively accessible and moderately priced. The doping process involves minimal amounts of Cu precursor, typically ranging from 1 to 5% by weight percentage. The synthesis process demonstrated a competitive cost structure compared to other photocatalysts. For instance: $BiVO_4$-based composites involving complex heterojunctions or co-catalysts often exceed RM 10.00 per gram due to additional material and processing requirements. Advanced catalysts such as $BiVO_4$-rGO hybrids require graphene oxide precursors, significantly increasing material costs to over RM 15 per gram. The hydrothermal method employed for synthesizing Cu-doped $BiVO_4$ is energy-intensive but offers high yields and superior material properties, such as controlled crystallite size and phase purity. The operational costs associated with maintaining a reaction temperature of 180 °C for 15 h are a significant factor. The operational energy requirement for photocatalytic applications is notably low due to the catalyst's ability to function under low-intensity UV light. Using a low-power (13 W) UV lamp significantly reduces electricity costs, making this catalyst ideal for low-energy, environmentally friendly applications. Additionally, the demonstrated stability and reusability of the Cu-doped $BiVO_4$ catalyst, with minimal loss of activity over three cycles, further enhance its cost-effectiveness by reducing the need for frequent material replacement. Table 3 depicts the estimated cost associated with the synthesis of the 3% Cu-doped $BiVO_4$. To further enhance the cost-efficiency of the synthesis process, several strategies can be explored. Bulk procurement of raw materials, such as $Bi(NO_3)_3 \cdot 5H_2O$ and NH_4VO_3, could significantly reduce material expenses due to economies of scale. Optimizing energy consumption by refining the synthesis process, for instance, by employing lower-temperature calcination or shorter reaction times, may decrease production costs without compromising the quality of the catalyst. Additionally, investigating renewable or waste-derived precursors for raw materials could provide a sustainable and cost-effective alternative, aligning with the growing emphasis on green chemistry. These approaches could further improve the economic viability of Cu-doped $BiVO_4$ for large-scale environmental remediation applications.

Photocatalyst	Synthetic method	Degradation efficiency (%)/time	References
Tb-doped $BiVO_4$	Hydrothermal	98.2%/150 min under visible light	21
Fe-loaded $BiVO_4$	Hydrothermal	81%/30 min under visible light	60
Mesoporous silica/$BiVO_4$	Ultrasonic	90.8%/60 min under visible light irradiation	62
$BiVO_4$/$BiPO_4$/rGO	Hydrothermal	94.4%/100 min under visible light irradiation	61
Mo-doped $BiVO_4$	Precipitation	88.57%/120 min under visible light irradiation	63
Cu-doped $BiVO_4$	Hydrothermal	95%/150 min under visible light irradiation	64
Al-doped $BiVO_4$	Hydrothermal	85%/120 min under visible light irradiation	65
Ni-doped $BiVO_4$	Hydrothermal	84.77%/180 min under visible light irradiation	66
1 wt% Cu-doped $BiVO_4$	Hydrothermal	85%/180 min under low-intensity UV light irradiation	This study

Table 2. MB degradation performance using various $BiVO_4$ based photocatalysts.

Item	Quantity (per batch)	Unit cost (RM)	Total cost (RM)	Notes
Raw materials				
$Bi(NO_3)_3 \cdot 5H_2O$	3.3954 g	RM 2.38/g	8.08	Bi source
NH_4VO_3	0.8189 g	RM 1.25/g	1.02	V source
$CuSO_4 \cdot 5H_2O$	0.101 g	RM 2.75/g	0.28	Cu dopant source
Total raw material cost			9.38	
Synthesis process				
Hydrothermal heating (180 °C)	1.5 kWh × 15 h = 22.5 kWh	RM 0.24 per kWh*	5.40	Energy cost for autoclave operation
Deionized water	200 mL	RM 0.01/mL	2.00	For dissolving reagents and washing catalyst
Ethanol (for washing)	20 mL	RM 0.11/mL	2.20	For catalyst washing
Drying	1.5 kWh × 12 h = 18.0 kWh	RM 0.24 per kWh*	4.32	Energy cost for oven operation
Calcination	3.0 kWh × 4 h = 12.0 kWh	RM 0.24 per kWh*	2.88	Energy cost for box furnace operation
Total synthesis cost			16.80	
Equipment depreciation				
Teflon-lined autoclave usage	–	–	0.20	Based on estimated equipment depreciation per batch
Centrifuge/filtration setup	–	–	0.10	Equipment for recovery and filtration
Total equipment cost			0.30	
Overall cost			26.48	Per batch (3.5 g photocatalyst yield)

Table 3. Estimated costs involved in the synthesis of 1% Cu-doped $BiVO_4$. *Refer to the Sarawak Energy tariff rate.
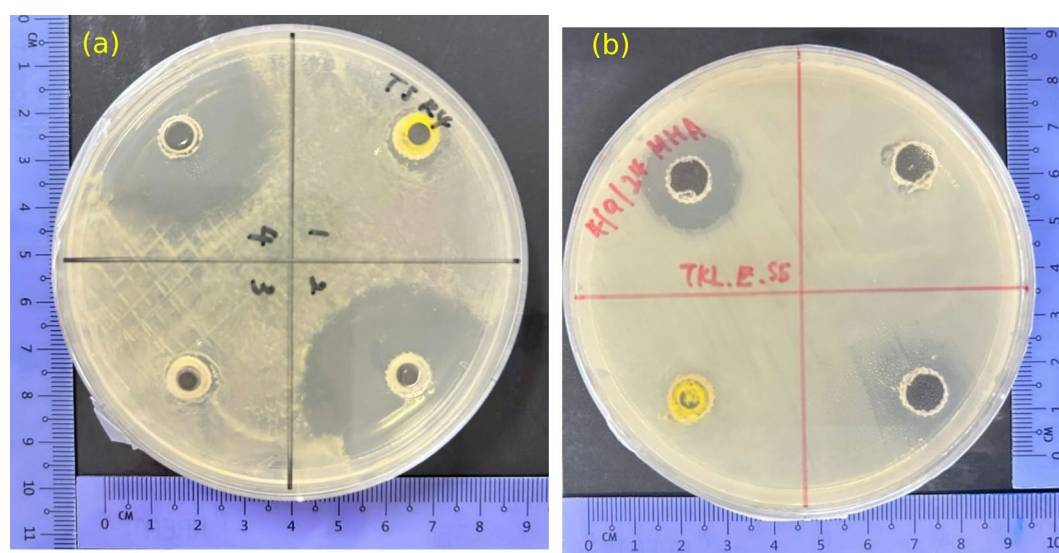

Fig. 13. Disk diffusion test for antibacterial activity. (**a**) *E.coli* (**b**) *S. aureus*.

To assess the economic robustness of synthesizing 1 wt% Cu-doped $BiVO_4$, a Monte Carlo simulation was performed using MATLAB R2023a. The simulation incorporated ± 10% variability in key cost inputs, including electricity tariff (RM 0.24/kWh), chemical costs, and equipment depreciation, based on market fluctuations. A total of 10,000 iterations were run to evaluate how these uncertainties affect the estimated cost per gram of catalyst. The resulting probability distribution shown in Fig. S3 follows a near-normal shape, indicating that the cost estimation model is statistically stable. The mean cost per gram was RM 7.59, with a standard deviation of RM 0.42. The 95% confidence interval (CI) ranged from RM 6.85 to RM 8.43, suggesting that the cost remains within economically viable margins even when input costs fluctuate moderately.

Antibacterial test

The antibacterial performance of the 1 wt% Cu-doped $BiVO_4$ against *E. coli* and *S. aureus* was evaluated in dark conditions with results compared to a control (95% ethanol) and positive controls (chloramphenicol and streptomycin) as shown in Fig. 13a and b, respectively. The 1 wt% Cu-doped $BiVO_4$ exhibited moderate antibacterial activity, with inhibition zones of 7.5 ± 0.79 mm for *E. coli* and 12.6 ± 0.40 mm for *S. aureus*, which were lower than those produced by the positive controls (chloramphenicol: 17.8 ± 3.90 mm for *E. coli* and

Sample	E. coli	S. aureus
1 wt% Cu-doped BiVO$_4$	7.5 ± 0.79	12.6 ± 0.40
Control	9.5 ± 1.50	10.5 ± 0.50
Chloramphenicol	17.8 ± 3.90	30.8 ± 3.30
Streptomycin	20.5 ± 1.20	39.9 ± 1.70

Table 4. Inhibition zone (mm) for the 1 wt% Cu-doped BiVO$_4$.

30.8 ± 3.30 mm for *S. aureus*; streptomycin: 20.5 ± 1.20 mm for *E. coli* and 39.9 ± 1.70 mm for *S. aureus*) as shown in Table 4.

Notably, the ethanol control showed a slightly larger inhibition zone against *E. coli* (9.5 ± 1.50 mm) than 1 wt% Cu-doped BiVO$_4$, while the photocatalyst had a marginally better effect against *S. aureus* (12.6 ± 0.40 mm vs. 10.5 ± 0.50 mm). In previous studies of polydopamine-rGO/BiVO$_4$, antibacterial test performed under the presence of light will significantly increase its ability to inhibit the growth of bacteria zone[67]. *S. aureus*, has a thicker peptidoglycan layer but lacks the outer membrane present in Gram-negative bacteria like *E. coli*. This structural difference makes *S. aureus* more susceptible to the penetration and action of nanoparticles[68]. Additionally, the mechanisms by which nanoparticles exert their antibacterial effects, such as oxidative stress induction and metal ion release, are more effective against Gram-positive bacteria[69]. Doping also accounts for the effectiveness of the antibacterial property's possess by the catalyst, where previous study revealed that Al-doped BiVO$_4$ performs better than bare BiVO$_4$[70].

It is important to note that the antibacterial tests in this study were conducted in dark conditions, thereby isolating the effects of Cu doping and associated structural defects without the contribution of photocatalytically generated ROS under light irradiation. The improved antibacterial activity can therefore be attributed to the presence of Cu-induced oxygen vacancies and lattice distortions, which are known to enhance the interaction between bacterial membranes and the catalyst surface. Defect engineering has been shown to modulate the electronic structure of oxide semiconductors by creating localized states that can act as shallow traps, improving surface reactivity. Similar observations were made previously, where defect-rich catalysts exhibited superior antibacterial activity through increased ROS generation and improved surface interactions[71,72]. Although ROS formation under visible light was not examined here, these findings provide a strong mechanistic context for the enhanced antibacterial performance of Cu-doped BiVO$_4$.

Conclusion

In this study, 1 wt% Cu-doped BiVO$_4$ photocatalyst was synthesized via a cost-effective hydrothermal method and evaluated for its photocatalytic and antibacterial properties. The incorporation of Cu significantly enhanced the photocatalytic degradation of MB under low-intensity UV light, achieving an 85% degradation efficiency within 180 min. This improvement was attributed to band gap narrowing, enhanced charge separation, and the generation of ROS, such as ·OH and ·O$_2^-$. The material also exhibited strong antibacterial activity against *S. aureus*, driven by photocatalytic ROS generation and the release of Cu^{2+} ions, making it a dual-functional material for environmental remediation. The catalyst demonstrated excellent reusability, retaining over 92% of its initial photocatalytic efficiency after three cycles, confirming its structural and functional stability. Cost analysis revealed that the material could be produced at RM 7.57 per gram, making it economically viable for large-scale applications. Moreover, the Cu-doped BiVO$_4$ outperformed many reported BiVO$_4$-based photocatalysts, highlighting its potential for practical deployment in energy-efficient pollutant degradation and microbial disinfection. This study serves as a preliminary investigation into the dual-functional properties of Cu-doped BiVO$_4$, focusing on fundamental synthesis, characterization, and performance assessment. The influence of common inorganic ions (e.g., CO$_3^{2-}$, Cl$^-$, Na$^+$, Ca^{2+}), which are prevalent in real wastewater and can quench reactive radicals or compete for active sites, was not evaluated. Future studies will expand upon this work by systematically examining the effects of these ions to better establish the applicability of Cu-doped BiVO$_4$ for large-scale water remediation. Herein, this study establishes Cu-doped BiVO$_4$ as a promising photocatalyst with exceptional multifunctional capabilities, aligning with the goals of sustainable and scalable environmental solutions.

Data availability

Data is provided within the manuscript or supplementary information files.

References

1. Jorge, A. M. S., Athira, K. K., Alves, M. B., Gardas, R. L. & Pereira, J. F. B. Textile dyes effluents: A current scenario and the use of aqueous biphasic systems for the recovery of dyes. *J. Water Process Eng.* **55**, 104125 (2023).
2. Jeffrey, K. B. et al. Sustainable dye wastewater treatment: Utilizing duckweed-derived adsorbents for efficient methylene blue removal. *Biomass Convers. Biorefin.* https://doi.org/10.1007/s13399-024-06432-1 (2024).
3. Zheng, A. L. T., Boonyuen, S., Ohno, T. & Andou, Y. Hydrothermally reduced graphene hydrogel intercalated with divalent Ions for dye adsorption studies. *Processes* **9**, 169 (2021).
4. Li, X. et al. Challenges of photocatalysis and their coping strategies. *Chem. Catal.* **2**, 1315–1345 (2022).

5. Yan, Z. et al. Photocatalysis for synergistic water remediation and H2 production: A review. *Chem. Eng. J.* **472**, 145066 (2023).
6. Kumari, H. et al. A review on photocatalysis used for wastewater treatment: Dye degradation. *Water Air Soil Pollut.* **234**, 349 (2023).
7. Shanmugam, P. et al. Hydrothermal synthesis and photocatalytic application of ZnS–Ag composites based on biomass-derived carbon aerogel for the visible light degradation of methylene blue. *Environ. Geochem. Health* **46**, 92 (2024).
8. Zheng, A. L. T., Sabidi, S., Ohno, T., Maeda, T. & Andou, Y. Cu2O/TiO2 decorated on cellulose nanofiber/reduced graphene hydrogel for enhanced photocatalytic activity and its antibacterial applications. *Chemosphere* **286**, 131731 (2022).
9. Zheng, A. L. T. et al. Rare earth elements for enhancing photocatalysis in pollutant degradation and water treatment. *Int. J. Environ. Sci. Technol.* **22**, 7247–7270 (2024).
10. Zheng, A. L. T. & Andou, Y. Hybrid three-dimensional (3D) graphene architectures for photocatalysis of noxious pollutants. In *Green Nanoarchitectonics* (ed. Pal, K.) 47–72 (Jenny Stanford Publishing, New York, 2022). https://doi.org/10.1201/9781003318606-3.
11. Zheng, A. L. T., Ohno, T. & Andou, Y. Recent progress in photocatalytic efficiency of hybrid three-dimensional (3D) graphene architectures for pollution remediation. *Top. Catal.* **65**, 1634–1647 (2022).
12. Ansari, A. S., Azzahra, G., Nugroho, F. G., Mujtaba, M. M. & Ahmed, A. T. A. Oxides and metal oxide/carbon hybrid materials for efficient photocatalytic organic pollutant removal. *Catalysts* **15**, 134 (2025).
13. Sun, K. et al. A review on conductive polymers-modified TiO2 photocatalyst for environmental remediation. *J. Environ. Chem. Eng.* **13**, 116518 (2025).
14. Zhang, Y., Li, H. & Yin, D. Recent progress in bismuth vanadate-based photocatalysts for photodegradation applications. *Nanomaterials* **15**, 331 (2025).
15. Helal, A., Yu, J., Ghanem, M. A., Labib, A. A. & El-Sheikh, S. M. Boosting the photocatalytic activity of bismuth vanadate (BiVO4) via optimization of the internal polarization. *J. Mol. Struct.* **1312**, 138553 (2024).
16. Kamble, G. S. et al. BiVO4 as a sustainable and emerging photocatalyst: Synthesis methodologies, engineering properties, and its volatile organic compounds degradation efficiency. *Nanomaterials* **13**, 1528 (2023).
17. Nedy, T. U. A. et al. Bismuth vanadate modified glassy carbon electrode for sensitive electrochemical antibiotic detection. *J. Nanopart. Res.* **27**, 86 (2025).
18. Zheng, A. L. T. et al. Recent advances in ultrasensitive electrochemical sensors and biosensors for determination of antibiotics in environment samples. *Clean Technol. Environ. Policy* **27**, 549–576 (2025).
19. Zheng, A. L. T., Teo, E. Y. L., Yiu, P. H., Boonyuen, S. & Andou, Y. Emerging trends in functional materials for electrochemical sensors in nicotine determination. *Anal. Sci.* **40**, 1933–1946 (2024).
20. Zheng, A. L. T. et al. Biochar-based electrochemical sensors: A tailored approach to environmental monitoring. *Anal. Sci.* **41**, 715–735 (2025).
21. Chen, W.-S., Wu, M.-H. & Wu, J.-Y. Effects of Tb-doped BiVO4 on degradation of methylene blue. *Sustainability* **15**, 6994 (2023).
22. Abdelraouf, H. et al. Gd-BiVO4 photocatalyst for organic contaminants removal: Short-term synthesis at sub-100 °C and enhanced sunlight-driven photocatalytic activity. *Process Saf. Environ. Prot.* **168**, 892–906 (2022).
23. Maran, M. A. et al. Assessing the photocatalytic performance of hydrothermally synthesized Fe-doped BiVO4 under low-intensity UV irradiation. *Arab. J. Sci. Eng.* https://doi.org/10.1007/s13369-025-10278-8 (2025).
24. Zhang, B. et al. Doping strategy to promote the charge separation in BiVO4 photoanodes. *Appl. Catal. B* **211**, 258–265 (2017).
25. Manikantan, K., Shanmugasundaram, K. & Thirunavukkarasu, P. Enhanced photocatalytic dye degradation and hydrogen evolution performance of Cu encapsulated BiVO4 under visible light irradiation. *Chem. Phys. Impact* **6**, 100178 (2023).
26. Nissi, J. R., Bincy, T. S., Prajeesh, S., Vidhya, B. & Murugan, S. Facile synthesis of Cu-doped BiVO4 using domestic microwave-assisted chemical precipitation method with fleeting time of microwave irradiation for the photocatalytic application. *Inorg. Nano-Met. Chem.* https://doi.org/10.1080/24701556.2023.2240765 (2023).
27. Tian, Y., Que, D., Guan, R. & Shi, W. SiO2 template-modified and Cu-doped BiVO4 with high visible-light photocatalytic performance: Preparation and first-principles study. *Mater. Today Commun.* **32**, 103954 (2022).
28. Li, J., Ma, Y., Xu, Y., Li, P. & Guo, J. Enhanced photocatalytic degradation activity of Z-scheme heterojunction BiVO4/Cu/g-C3N4 under visible light irradiation. *Water Environ. Res.* **93**, 2010–2024 (2021).
29. Shah, S. S., Ramos, B. & Teixeira, A. C. S. C. Adsorptive removal of methylene blue dye using biodegradable superabsorbent hydrogel polymer composite incorporated with activated charcoal. *Water (Basel)* **14**, 3313 (2022).
30. Zheng, A. L. T. et al. Accessing the anti-microbial activity of cyclic peptide immobilized on reduced graphene oxide. *Mater. Lett.* **304**, 130621 (2021).
31. Farrag, H. N. et al. Novel cyclic undecapeptides immobilized on reduced graphene oxide surface for enhanced antibacterial properties. *Int. J. Environ. Sci. Technol.* **21**, 1481–1492 (2024).
32. Bhatti, I. N., Dhaka, R. S. & Pramanik, A. K. Effect of Cu^{2+} substitution in spin–orbit coupled Sr2Ir$_{1-x}$Cu$_x$O4: Structure, magnetism, and electronic properties. *Phys. Rev. B* **96**, 144433 (2017).
33. Merupo, V.-I. et al. Structural and optical characterization of ball-milled copper-doped bismuth vanadium oxide (BiVO4). *CrystEngComm* **17**, 3366–3375 (2015).
34. Phuruangrat, A. et al. Characterization and photocatalytic properties of BiVO4 synthesized by combustion method. *J. Mol. Struct.* **1274**, 134420 (2023).
35. Chen, P. A promising strategy to fabricate the Cu/BiVO4 photocatalysts and their enhanced visible-light-driven photocatalytic activities. *J. Mater. Sci. Mater. Electron.* **27**, 2394–2403 (2016).
36. Sena, H. & Fuji, M. Band gap engineering of semiconductors and ceramics by severe plastic deformation for solar energy harvesting. *Mater. Trans.* **64**, 1497–1503 (2023).
37. Zainullina, V. M., Zhukov, V. P. & Korotin, M. A. Influence of oxygen nonstoichiometry and doping with 2*p*-, 3*p*-, 6*p*- and 3*d*-elements on electronic structure, optical properties and photocatalytic activity of rutile and anatase: Ab initio approaches. *J. Photochem. Photobiol. C* **22**, 58–83 (2015).
38. Niu, X. et al. The regulating effect of boron doping and its concentration on the photocatalytic overall water splitting of a polarized g-C3N5 material. *Phys. Chem. Chem. Phys.* **25**, 8592–8599 (2023).
39. Choudhury, B., Dey, M. & Choudhury, A. Defect generation, d-d transition, and band gap reduction in Cu-doped TiO2 nanoparticles. *Int. Nano Lett.* **3**, 25 (2013).
40. He, B. et al. Fabrication of porous Cu-doped BiVO4 nanotubes as efficient oxygen-evolving photocatalysts. *ACS Appl. Nano Mater.* **1**, 2589–2599 (2018).
41. Bakhtiarnia, S. et al. Preparation of sputter-deposited Cu-doped BiVO4 nanoporous thin films comprised of amorphous/crystalline heterostructure as enhanced visible-light photocatalyst. *Appl. Surf. Sci.* **608**, 155248 (2023).
42. Guo, Y., Siretanu, I., Mugele, F., Mul, G. & Mei, B. pH-Dependent photocatalytic performance of faceted BiOBr semiconductor particles in degradation of dyes. *Mol. Catal.* **553**, 113753 (2024).
43. Hanafi, M. F. & Sapawe, N. Effect of pH on the photocatalytic degradation of remazol brilliant blue dye using zirconia catalyst. *Mater. Today Proc.* **31**, 260–262 (2020).
44. Mohammadi, A. A. et al. The using of plain PAC and PAC impregnated with MgO and Fe2O3 as catalysts for the degradation of cationic dyes: Homogenous and heterogeneous ozonation. *Turk. J. Fish Aquat. Sci.* **24**, 1–13 (2024).
45. Singla, S., Devi, P. & Basu, S. Highly effectual photocatalytic remediation of tetracycline under the broad spectrum of sunlight by novel BiVO4/Sb2S3 nanocomposite. *Catalysts* **13**, 731 (2023).

16

46. Yoshida, K. Role of nanoparticle size in the photocatalytic degradation of pollutants. *J. Chem.* **3**, 12–20 (2024).

47. Ali, M. H. H., Abdelkarim, M. S. & Al-Afify, A. D. G. Characterization and photodegradation of methylene blue dye using bio-synthesized cerium oxide nanoparticles with Spirulina platensis extract. *Discov. Appl. Sci.* **6**, 94 (2024).

48. de Mendonça, V. R., Mourão, H. A. J. L., Malagutti, A. R. & Ribeiro, C. The role of the relative dye/photocatalyst concentration in TiO₂ assisted photodegradation process. *Photochem. Photobiol.* **90**, 66–72 (2014).

49. Dahiya, A. & Patel, B. K. Photocatalytic degradation of organic dyes using heterogeneous catalysts. In *Photocatalytic Degradation of Dyes* (eds Shah, M. et al.) 43–90 (Elsevier, 2021). https://doi.org/10.1016/B978-0-12-823876-9.00012-3.

50. Meng, S., Ogawa, T., Okumura, H. & Ishihara, K. N. Enhanced photocatalytic activity of BiVO₄/Bi₂S₃/SnS₂ heterojunction under visible light. *Catalysts* **10**, 1294 (2020).

51. Mureithi, A. W., Sun, Y., Mani, T., Howell, A. R. & Zhao, J. Impact of hole scavengers on photocatalytic reduction of nitrobenzene using cadmium sulfide quantum dots. *Cell Rep. Phys. Sci.* **3**, 100889 (2022).

52. Ranjith, K. S. & Rajendra Kumar, R. T. Regeneration of an efficient, solar active hierarchical ZnO flower photocatalyst for repeatable usage: Controlled desorption of poisoned species from active catalytic sites. *RSC Adv.* **7**, 4983–49924 (2017).

53. Kamo, A., Ates Sonmezoglu, O. & Sonmezoglu, S. Ternary zinc–tin-oxide nanoparticles modified by magnesium ions as a visible-light-active photocatalyst with highly strong antibacterial activity. *Nanoscale Adv.* **6**, 6008–6018 (2024).

54. Kamo, A., Sonmezoglu, O. A. & Sonmezoglu, S. Highly efficient photocatalyst based on Zn₂₋ₓBaₓSnO₄ alloying nanoparticles with enhanced photocatalytic activity. *Inorg. Chem. Commun.* **174**, 114080 (2025).

55. González, S. & Jaramillo-Fierro, X. Density functional theory study of methylene blue demethylation as a key step in degradation mediated by reactive oxygen species. *Int. J. Mol. Sci.* **26**, 1756 (2025).

56. Breault, T. M. & Bartlett, B. M. Composition dependence of TiO₂:(Nb,N)-*x* compounds on the rate of photocatalytic methylene blue dye degradation. *J. Phys. Chem. C* **117**, 8611–8618 (2013).

57. Houas, A. Photocatalytic degradation pathway of methylene blue in water. *Appl. Catal. B* **31**, 145–157 (2001).

58. Khan, I. et al. Review on methylene blue: Its properties, uses, toxicity and photodegradation. *Water (Basel)* **14**, 242 (2022).

59. Yang, C. et al. Highly efficient photocatalytic degradation of methylene blue by P2ABSA-modified TiO₂ nanocomposite due to the photosensitization synergetic effect of TiO₂ and P2ABSA. *RSC Adv.* **7**, 23699–23708 (2017).

60. Chala, S., Wetchakun, K., Phanichphant, S., Inceesungvorn, B. & Wetchakun, N. Enhanced visible-light-response photocatalytic degradation of methylene blue on Fe-loaded BiVO₄ photocatalyst. *J. Alloys Compd.* **597**, 129–135 (2014).

61. Yang, F. et al. Photocatalytic degradation of methylene blue over BiVO₄/BiPO₄/rGO heterojunctions and their artificial neural network model. *J. Alloys Compd.* **960**, 170716 (2023).

62. El-Hakam, S. A. et al. Application of nanostructured mesoporous silica/bismuth vanadate composite catalysts for the degradation of methylene blue and brilliant green. *J. Market. Res.* **18**, 1963–1976 (2022).

63. Liu, B. et al. Preparation and characterization of Mo doped in BiVO₄ with enhanced photocatalytic properties. *Materials* **10**, 976 (2017).

64. Regmi, C. et al. Understanding the multifunctionality in Cu-doped BiVO₄ semiconductor photocatalyst. *J. Environ. Sci.* **75**, 84–97 (2019).

65. Cao, Y. et al. Investigation on Al³⁺ and Al₂O₃ Coexist in BiVO₄ for efficient methylene blue degradation: insight into surface states and charge separation. *Langmuir* **37**, 7617–7624 (2021).

66. Pham, V. T., Dao, T. B. T., Tran, T. K. N., Tran, N. Q. & Bach, L. G. Synthesis of nickel-doped BiVO₄ materials by hydrothermal method and evaluate the photocatalytic ability to decompose methylene blue under visible light. *Vietnam J. Sci. Technol.* https://doi.org/10.15625/2525-2518/17140 (2024).

67. Li, B. et al. Visible-light-driven antimicrobial activity and mechanism of polydopamine-reduced graphene oxide/BiVO₄ composite. *Int. J. Mol. Sci.* **23**, 7712 (2022).

68. El-Masry, R. M. et al. Evaluation of the antimicrobial activity of ZnO nanoparticles against enterotoxigenic *Staphylococcus aureus*. *Life* **12**, 1662 (2022).

69. Arunachalam, K., Pandurangan, P., Shi, C. & Lagoa, R. Regulation of *Staphylococcus aureus* virulence and application of nanotherapeutics to eradicate *S. aureus* infection. *Pharmaceutics* **15**, 310 (2023).

70. Vicas, C. S., Keerthiraj, N., Byrappa, N. & Byrappa, K. Hydrothermally synthesized Al-doped BiVO₄ as a potential antibacterial agent against methicillin-resistant *Staphylococcus aureus*. *Environ. Eng. Res.* **24**, 566–571 (2018).

71. Kamo, A., Ates Sonmezoglu, O. & Sonmezoglu, S. Unraveling the effects of strain-induced defect engineering on the visible-light-driven photodynamic performance of Zn₂SnO₄ nanoparticles modified by larger barium cations. *ACS Appl. Bio Mater.* **7**, 8656–8670 (2024).

72. Muhammad, P. et al. Defect engineering in nanocatalysts: From design and synthesis to applications. *Adv. Funct. Mater.* **34**, 2314686 (2024).

Acknowledgements

Author contributions

TKL wrote the main manuscript and was responsible for conducting formal analysis and investigation. ALTZ provided supervision and was responsible for writing—reviewing and editing and project administration. THY and SRS were responsible for formal analysis. KWKS and ELTC were responsible for investigation. YA was responsible for supervision and for writing—reviewing and editing. TKB was responsible for writing—reviewing and editing.

Funding

Declarations

Competing interests

The authors declare no competing interests.

Consent for publication

All authors reviewed and agreed to the final manuscript for publication.

Additional information

Supplementary Information The online version contains supplementary material available at https://doi.org/1 0.1038/s41598-025-17994-z.

Correspondence and requests for materials should be addressed to A.L.T.Z.

Reprints and permissions information is available at www.nature.com/reprints.

Publisher's note Springer Nature remains neutral with regard to jurisdictional claims in published maps and institutional affiliations.